JOURNAL OF GEOPHYSICAL RESEARCH: SPACE PHYSICS, VOL. 118, 5379–5391, doi:10.1002/jgra.50480, 2013

Modeling the ionospheric *E* and *F1* regions: Using SDO-EVE observations as the solar irradiance driver

Jan J. Sojka,[1] Joseph Jensen,[1] Michael David,[1] Robert W. Schunk,[1] Tom Woods,[2] and Frank Eparvier[2]

Received 1 March 2013; revised 13 May 2013; accepted 29 July 2013; published 23 August 2013.

[1] Over the altitude range of 90–150 km, in dayside nonauroral regions, ionization is controlled almost entirely by solar ultraviolet irradiance; the response time for ionization during solar exposure is almost instantaneous, and likewise, the time scale for recombination into neutral species is very fast when the photoionizing source is removed. Therefore, if high-resolution solar spectral data are available, along with accurate ionization cross sections as a function of wavelength, it should be possible to model this ionospheric region with greater accuracy. The Extreme Ultraviolet Variability Experiment (EVE) instrument on the National Aeronautics and Space Administration Solar Dynamics Observatory (SDO) satellite, launched in February 2010, is intended to provide just such solar data, at high resolution in both wavelength and time cadence. We use the Utah State University time-dependent ionospheric model to assess the sensitivity in modeling that this solar irradiance data provide, under quiet solar conditions as well as during X-class flares. The sensitivity studies show that the *E* and *F1* regions, as well as the valley region, are strongly dependent upon wavelength in both electron density and ion composition.

Citation: Sojka, J. J., J. Jensen, M. David, R. W. Schunk, T. Woods, and F. Eparvier (2013), Modeling the ionospheric *E* and *F1* regions: Using SDO-EVE observations as the solar irradiance driver, *J. Geophys. Res. Space Physics*, *118*, 5379–5391, doi:10.1002/jgra.50480.

1. Introduction

[2] Modeling of the *E* and *F1* regions is less advanced than the modeling of the *F2* region, not because the physical processes are not well understood but because the input parameters are less well specified. Over most of the globe, the *E* and *F1* region is created by solar irradiance during the daytime (although in auroral regions, energetic particle precipitation can be a significant contributor). The most important wavelength band for ionizing in this altitude range is the X-ray ultraviolet (XUV), approximately 1–30 nm. These photons ionize O_2, N_2, O, and to a lesser degree, NO, but in addition to these primary ionizations, the photoelectrons have enough energy to produce secondary ionizations. This cascade of ionization depends critically upon the distribution of irradiance as a function of wavelength throughout the XUV band. A lesser source of ionization for the *E* layer is the ionization of O_2 by photons between 90 and 103 nm. In this case, there is no secondary photoelectron ionization because the photoelectrons are not energetic enough.

[3] *Lilensten et al.* [1989] demonstrated that previous modeling of the cascade of ionization was inadequate and concluded, in general, a full photoelectron transport model would be needed to generate the correct altitude distribution of secondary ionizations. They also pointed out that the obstacle to developing such a model was the lack of high-resolution XUV observations that would allow the appropriate photoionization and photoelectron profiles to be determined.

[4] *Buonsanto et al.* [1992] compared two different *E* and *F1* region models with electron density profiles obtained from the incoherent scatter radar (ISR) device at Millstone Hill in Massachusetts. Using a formulation of the XUV input spectrum, which was significantly improved, but which still lacked the desired level of wavelength resolution, the models failed to match the ISR observations. Again the lack of resolution in the specification of the XUV spectrum was pointed to as the main reason for the failure.

[5] *Titheridge* [1996] developed an independent approach to modeling the *E* and *F* regions based on decades of ionosonde measurements. In his modeling work, he demonstrated how the altitude profile of this region depends on the XUV spectrum as well as on the photoelectron ionization. However, a lack of adequate XUV irradiance measurements is again a limitation of this work.

[6] *Solomon et al.* [2001] used new solar irradiance measurements made by the Student Nitric Oxide Explorer (SNOE) with a three-channel X-ray photometer covering spectral ranges of 2–7, 6–19, and 17–20 nm. The main finding from 2 years of SNOE observations was that the standard reference irradiance spectrum based on *Hinteregger et al.* [1981] needed to be scaled by factors of 5, 3.5, and 4.4 in the spectral ranges just mentioned. *Solomon et al.* [2001]

[1]Center for Atmospheric and Space Sciences, Utah State University, Logan, Utah, USA.
[2]LASP, University of Colorado Boulder, Boulder, Colorado, USA.

Corresponding author: J. J. Sojka, Center for Atmospheric and Space Sciences, Utah State University, 4405 Old Main Hill, Logan, UT 84322-4405, USA. (jan.sojka@usu.edu)

2169-9380/13/10.1002/jgra.50480

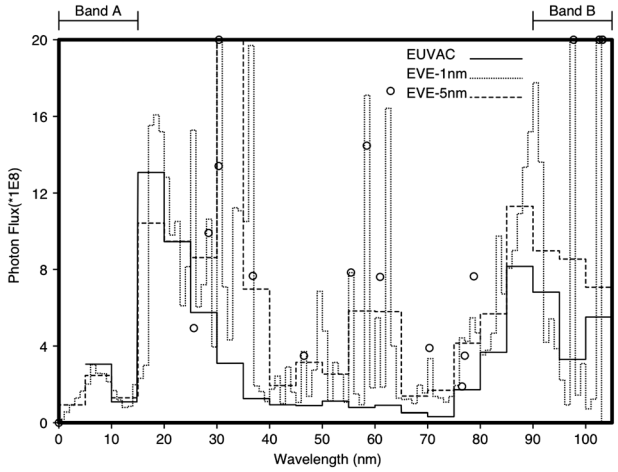

Figure 1. A graph of the solar photon flux (photons/cm^{2}s) obtained by EVE on 8 February 2012 in both the 1 and 5 nm bin format represented by dotted and dashed lines, respectively. Also included is the EUVAC 37 bin and line spectrum as a solid line; the EUVAC spectral lines are denoted by circles.

provided a revised comparison with the Millstone Hill ISR observations and found that using a factor of 4 scaling of the XUV irradiance could achieve excellent agreement with the observed electron densities in the *E* and *F1* regions.

[7] Since the SNOE mission, which ended in 1999, NASA has flown solar irradiance sensors of good spectral resolution on two satellite missions, thermosphere ionosphere mesosphere energetics and dynamics (TIMED) and Solar Dynamics Observatory (SDO). TIMED carried the solar extreme ultraviolet experiment (SEE) instrument, which on each 90 min orbit, measured the solar spectrum from 0.1 to 190 nm but with only broadbands below 27 nm. Currently, the Extreme Ultraviolet Variability Experiment (EVE) instrument observes, with a 10 s cadence, the XUV band from 0.1 to 7 nm and the spectrum from 6 to 106 nm with 0.02 nm bins and a true 0.1 nm resolution.

[8] In this study, we assess the value of the SDO-EVE spectral observations as a driver for modeling the *E* and *F1* regions. In section 2, the EVE observations are described; in section 3, we describe the ionospheric model used in the study. Section 4 will evaluate the EVE irradiances from an ionospheric simulation stance. The comparison of how the ionospheric simulation contrasts to that simulated by a standard semi-empirical irradiance model is given in section 4.1. Section 4.2 considers the sensitivity of the *E* and *F1* composition, density, and profile to uncertainties in the EVE spectrum. Section 4.3 considers the response of the *E* and *F1* ionospheric layers to X-class flares. In section 5, we discuss some other mechanisms not modeled in this study, and section 6 provides our conclusions regarding the strengths and weaknesses of the SDO-EVE observations as a driver for ionospheric modeling.

2. Ionizing Irradiance

2.1. General

[9] The solar photons that ionize the *E* and *F1* regions are in two separate parts of the XUV and extreme ultraviolet (EUV: 30–120 nm) spectrum. These are the photons with wavelength between 2 and 15 nm, which we will call Band A, and between 90 and 103 nm, which we will call Band B. Photons of a wavelength between these two bands do not generally penetrate to these lower altitudes; instead, they ionize the *F2* region. At a wavelength of 121.6 nm (Hydrogen Lyman Alpha), ionization of NO occurs, but this has significance primarily at *D* region altitudes (private communication, Vincent Eccles, 2012) and is not discussed in this study. Photons of wavelength less than 2 nm have very small ionization cross sections and hence will penetrate to altitudes below the *E* region.

2.2. SDO-EVE Observations

[10] This study would not be possible without the measurements of the XUV solar irradiance made by the EVE instrument aboard NASA's Solar Dynamics Observatory. This platform was launched in February 2010 as the current solar cycle 24 was beginning to ramp up. The EVE instrument, and its calibration, are well understood [see *Woods et al*., 2012; *Hock et al*., 2012]. A key aspect of the SDO satellite in geosynchronous orbit (GEO) is that it provides continuous solar observations with very few Earth eclipses. Irradiance products from EVE are available in a variety of wavelength resolutions and time cadences from the EVE website, http://lasp.colorado.edu/home/eve/data/data-access/. Three sensors of the EVE instrument are relevant in the present study. The sensor Multiple EUV Grating Spectrograph A (MEGS-A) is a spectrograph that provides 0.1 nm resolution in the wavelength range of 6–37 nm; MEGS-B is a spectrograph likewise providing 0.1 nm resolution in the range 37–106 nm. The MEGS data products provide the irradiance in 0.02 nm bins. The EUV SpectroPhotometer (ESP) Quadrant Diode (QD) provides the irradiance over the 0.1 to 7 nm band.

[11] This low resolution from ESP-QD is, at present, the weakest aspect in the effort to model the ionospheric *E* and *F1* region response to the solar spectral irradiance. Two facts compound the difficulty that this short-wavelength band of the spectrum presents for the purpose of ionospheric modeling: i) the XUV spectrum below 15 nm is known to be highly variable, with a strong dependence on solar conditions [see *Chamberlin et al*., 2007, 2008]; and ii) the *E* and *F1* region ionization cross sections change by more than two orders of magnitude over this spectral range. Hence, to create a 1 nm bin width EVE spectrum that begins at 1 nm and extends up to 105 nm, a spectral shape must be adopted for the ESP-QD 0.1 to 7 nm measurement. We have adopted a flat irradiance spectrum over this wavelength range. In Subsection 4.2.1, a discussion of how sensitive the *E* and *F1* region electron density is to this choice is presented.

[12] We have taken the EVE 0.1 nm resolution data and binned them to 1 and 5 nm length bins over the wavelength range of 0.1 nm to 105 nm and plotted them as found in Figure 1. As a reference, we have plotted the EVE data against the standard 37 bin and line EUVAC spectrum [*Richards et al*., 1994] for the day 8 February 2012. It can be seen that over the bands of interest that there are differences to the EUVAC model. In band A, there is no data in the EUVAC model in the 0.1 to 5 nm range, and in the 15–20 nm range, the EUVAC is 14% higher than the 5 nm resolution EVE data, while for band B, 90 to 105 nm,

the contributions from line emission is significant. Over the rest of the wavelength spectrum 20–90 nm, the EUVAC is lower than the 5 nm EVE data by 18%.

3. Ionospheric Model

[13] The time-dependent ionospheric model (TDIM) was initially developed as a midlatitude multi-ion $\left(NO^+, O_2^+, N_2^+, \text{and } O^+\right)$ model by *Schunk and Walker* [1973]. The time-dependent ion continuity and momentum equations were solved as a function of altitude for a corotating plasma flux tube including diurnal variations and all relevant *E* and *F* region processes. This model was extended to include high-latitude effects due to convection electric fields and auroral particle precipitation by *Schunk et al*. [1975, 1976]. A simplified ion energy equation was also added, which was based on the assumption that local heating and cooling processes dominate (valid below 500 km). The addition of plasma convection and particle precipitation models is described by *Sojka et al*. [1981a, 1981b]. *Schunk and Sojka* [1982] extended the ionospheric model to include ion thermal conduction and diffusion thermal heat flow. Also, the electron energy equation was included by *Schunk et al*. [1986], and consequently, the electron temperature is now rigorously calculated at all altitudes. The theoretical development of the TDIM is described by *Schunk* [1988], while comparisons with observations are discussed by *Sojka* [1989].

[14] The majority of the TDIM science studies emphasized the *F2* region. *Rasmussen et al*. [1988] considered the *E* region under auroral conditions of particle precipitation with an emphasis on evaluating the TDIM generated Hall and Pedersen conductivities. These conductivities are located in the *E* and *F1* altitude region. *Smithtro et al*. [2006] carried out studies of the TDIM's response to solar flares, in which the model's sensitivity to the solar irradiance wavelength dependence was important. To conduct simulations during solar flare conditions, a number of different irradiance models and their corresponding absorption and ionization cross sections were used, and the results were compared. This led to the TDIM being extended to better deal with high-resolution inputs of the XUV irradiance. The standard TDIM as described above used a wavelength spectrum consisting of 11 bins. This was augmented in the Smithtro study by two other standard wavelength representations: the 37 bin-and-line model of *Torr et al*. [1979], and a 20 bin representation of *Solomon et al*. [2001]. In addition, the FISM irradiance model of *Chamberlin et al*. [2007] is an option, as would be any other wavelength-dependent model for which the irradiance and cross sections can be specified.

[15] The three photon flux spectra shown in Figure 1 are the primary solar drivers to be used in the TDIM sensitivity study. In addition to ionization created by the photons, it is also necessary to account for photoelectrons producing secondary ionization. In the TDIM, as with most other ionospheric first principles physics models, this photoelectron ionization cascade is usually parameterized or based on a simple prescription. *Solomon et al*. [2001] showed that for their particular simulation comparison with a Millstone Hill Incoherent Scatter Radar *E* region profile, a factor of 4 increase of the photon ionization produced good agreement. In contrast, the PRIMO study summary [*Anderson et al*., 1998] found that in the *E* region, a factor of 2 provides reasonable agreement when used by five different ionospheric models. Another scheme is to use 35 eV as the average energy a photoelectron requires to create a further ionization [*Rasmussen et al*., 1988]. This scheme introduces a wavelength dependence on computing the secondary ionization. Thus, during a flare when the short wavelength X-rays are considerably enhanced, larger secondary ionization will be generated. In this study, the "35 eV" scheme is used.

[16] The main reason for adopting this scheme is that it will emphasize the additional ionization in the altitude region where most of the energetic photoelectrons are produced. This is in the *E* region, and in this region, it is also the case that the photoelectron mean free paths are short enough for their ionization and thermalization to be confined to this region. However, this scheme and the other two mentioned will need to be compared to results from a full photoelectron transport code incorporated in an ionospheric model. Comparison between the factor of 4 scaling and the 35 eV factor scheme in the TDIM can be summarized as lower Ne in the *E* region for the factor of 4 scaling by about 35%, while in the *F1* region (120–150 km), the factor of 4 scaling almost doubles the electron density.

[17] The EVE-5 nm irradiance is distributed over 22 bins, which correspond to the 20 bins of *Torr et al*. [1979], augmented by an additional bin at each end. This scheme is similar to that of the study by *Solomon et al*. [2001]. The 17 lines of the original *Torr et al*. [1979] scheme are redundant in this representation. We have included a graph of the cross sections for these 22 bins, with the exception of Lyman Alpha (bin 22), in Figures 2a and 2b, which contain the ionization cross sections for N_2 and O_2, respectively. The cross sections for these 21 bins were obtained from studies by *Richards et al*. [1994] and *Banks and Kockarts* [1973].

[18] In both of these bands, the ionization cross sections have a strong dependence on wavelength; in band A, the cross sections are smaller toward the shorter wavelengths, while in band B, the reverse is true, the cross sections being larger for the shorter wavelengths. A further difference between the two bands is that in band B, only primary ionizations occur, while in band A, the photoelectrons are released with enough energy to result in cascades of secondary ionizations. An additional complication comes from the fact that within band B, at wavelengths above 91 nm, only O_2 is ionized; neither N_2 nor O can be ionized by photons of wavelength longer than 91 nm. Therefore, the ionospheric composition in the *E* and *F1* regions depends also upon a complex set of competing chemical interactions.

[19] We also included the cross sections as they would appear in the 1 nm bin format [*Fennelly and Torr*, 1992] as well as the EUVAC 37 bin-and-line cross sections. The differences between the cross sections are very small for band A, but over band B, 90–105 nm, there are some differences in the ionization of oxygen which amounts to EUVAC having smaller cross sections over this range by 20%. The dashed circles in Figure 2 are the cross sections associated with the EUVAC 17 lines.

[20] The TDIM also requires several other inputs. The geomagnetic condition used in this study is quiet, Kp < = 1+. For the neutral atmosphere, we have used NRL-MSIS-2000 [*Picone et al*., 2002], and for the neutral winds, the Horizontal Wind Model (HWM93) is used [*Hedin et al*., 1991, 1994, 1996]. The location for which ionospheric

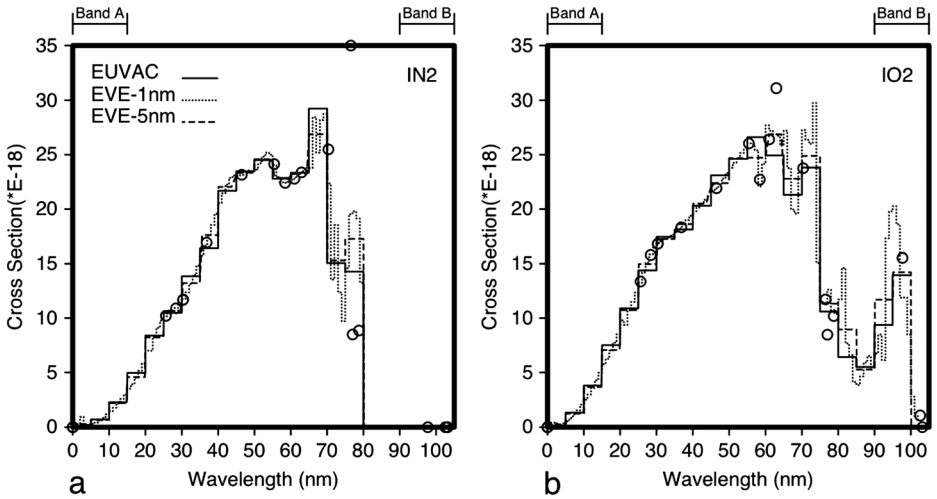

Figure 2. (a) Graph of the ionization of N_2 on the wavelength band of 0.01 to 105 nm. There are three representations of the cross section: the 1 nm bin width, the 5 nm bin width, and the 37 bin and line format. The 1 and 5 nm bins were found using the data from *Fennelly and Torr* [1992], and the 37 bin and line was taken from the study of *Richards et al*. [1994]. (b) Graph of the ionization of O_2 on the wavelength band of 0.01 to 105 nm.

simulations are performed is Bear Lake Observatory (BLO), in Utah (42°N, 111°W); at such a midlatitude location during quiet geomagnetic conditions, neither the magnetospheric convection electric field nor the auroral precipitation play a role.

4. Ionospheric Simulations

[21] The EVE irradiance measurements provide a comprehensive description of the solar XUV that creates the terrestrial dayside ionosphere. This enables comparisons of ionospheric simulations that are based on community standard semi-empirical solar irradiance inputs (section 4.1), a wavelength sensitivity study for the *E* and *F1* region (section 4.2), and a temporal response of the ionosphere to the 10 s EVE irradiance cadence of a flare (section 4.3). These comparisons and sensitivity studies quantify how the *E* and *F1* ionospheric layers have different dependencies on photoionization.

4.1. Midlatitude Noon Ionosphere

[22] In section 2, three solar irradiance spectra were presented; the EUVAC 37 bin and line solar photon flux spectrum, and two EVE spectra that were binned at 5 and 1 nm resolution. EUVAC is a widely used community standard. All three spectra are representative of the solar irradiance on the 8 February 2012. Three ionospheric simulations were carried out for this day using the TDIM model. In section 3, this model was described, and the key photoionization cross sections were contrasted in Figures 2a and 2b. Qualitatively, all three photon flux spectra and sets of cross sections are similar; however, several key differences in the subsequent TDIM ionospheres are noted.

[23] Figure 3a compares the noon time ionospheric profiles at the BLO, Utah location. The four left panels show the $NO^+, O_2^+, O^+,$ and electron density (Ne) profiles from the lower to upper panels, respectively. The lower three panels contrast the ionospheric composition, which is the key to defining the ionospheric layers; *F2* is dominated by O^+, the *F1* transition region of molecular to atomic dominance, and the *E* region which is molecular ion dominant. In Figure 3a, the density is plotted logarithmically since the ionospheric density ranges over three orders of magnitude from the *D* region to the peak density in the *F2* layer. To contrast the three ionospheric simulations, a percentage difference relative to the EUVAC driven simulation is shown in Figure 3b. Between 200 and 500 km, the three simulations differ in a systematic way with the 1 nm EVE driven simulation being 8% higher and the 5 nm EVE driven simulation being 15% higher in electron density. These *F2* region differences on the one hand may appear rather small; however, when cast in a more application relevant form, the ionosphere's total electron content (TEC), a different perspective can be obtained. The EUVAC driven noon simulation at BLO as shown in Figure 3 has a corresponding TEC of 11.7 tecu, while the EVE 1 nm and 5 nm driven simulations have TEC values of 12.4 and 13.0 tecu. Hence, the EVE (1 nm)-EUVAC difference is 0.7 tecu and the EVE (5 nm)-EUVAC difference is 1.3 tecu. (These differences have the same magnitude as the analysis uncertainties of the TEC derived from the GPS system world wide.)

[24] Between 100 and 200 km, the Figure 3 densities and percent differences vary in a different manner than in the *F2* layer. This altitude range spans the ionosphere *E* and *F1* region and the valley in between. Figure 4a shows this altitude region in detail with composition and electron density organized as in Figure 3a. In this ionospheric layer, the molecular ions are dominant with O_2^+ having a double peak structure over the range of 100–150 km and NO^+ having the dominant peak at 150 km. Between 150 and 200 km, the ionospheric composition is transitioning from molecular ion to atomic oxygen ions. The *E* region lies between 90 and 120 km and shows the largest TDIM simulation difference between the three solar irradiance drivers. In the *F2* region, the differences were systematic with the 1 nm EVE

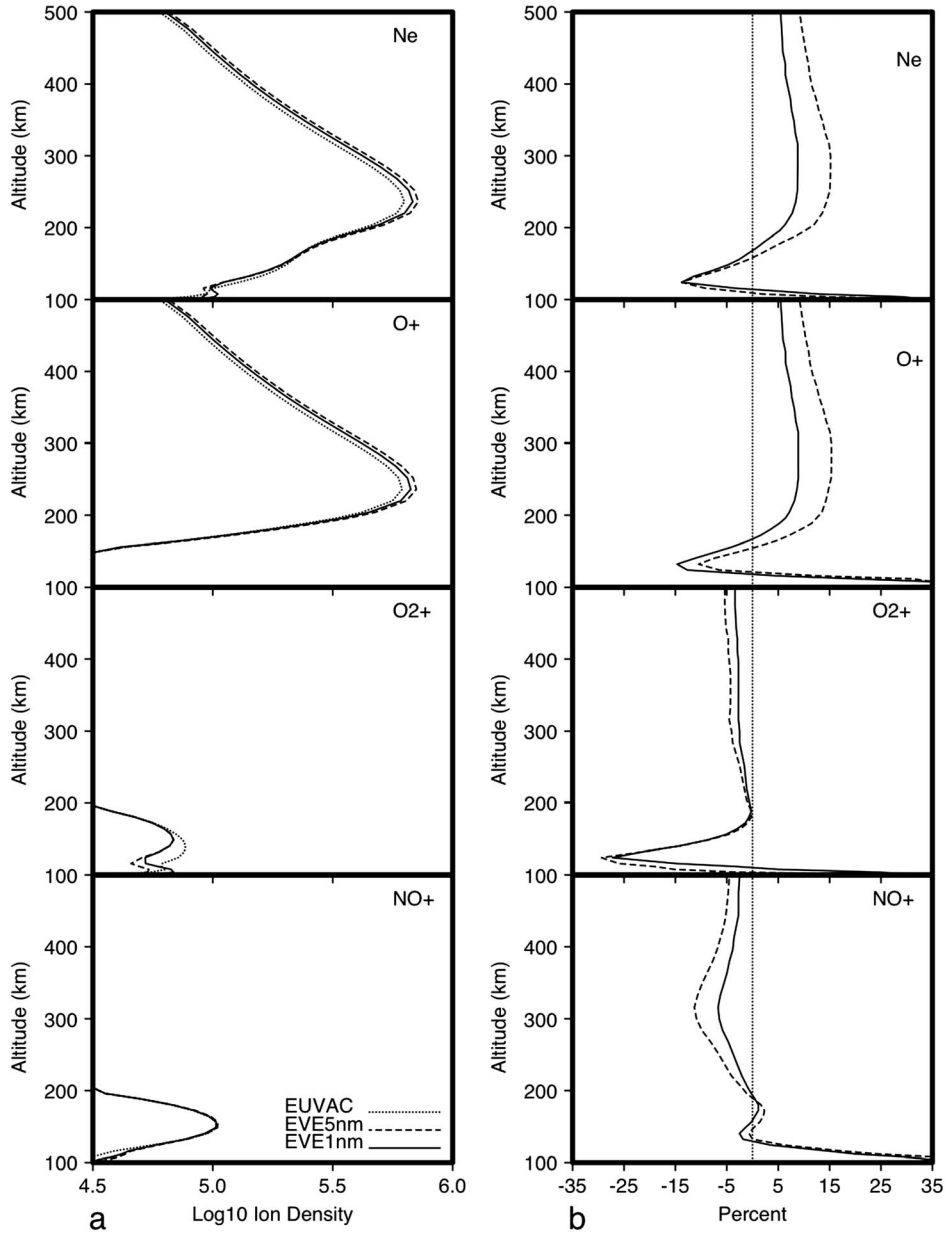

Figure 3. (a) TDIM ionospheric simulations for the EUVAC case (solid line), EVE-1 nm case (dotted line), and EVE-5 nm case (dashed line) for NO^+, O_2^+, O^+, and Ne, respectively, from bottom to top left panels. (b) Corresponding percentage differences. The percentage differences are in comparison to the EUVAC case. Each panel shows simulated profiles from 100 to 500 km for the BLO location at noon on 8 February 2012.

simulation being 8% larger and the 5 nm EVE simulation being 15% larger than the EUVAC case. This is no longer the case. In the valley region between the *E* and *F1* regions, centered at 120 km, both EVE driven simulations are lower than EUVAC for O_2^+, O^+ and Ne, see Figure 4b. The electron density difference in the valley reaches −15% in both EVE driven cases. However, in the *E* region below 110 km, the EVE driven cases are significantly larger, reaching percentages around 100% in all ion species and the electron density, see Figure 4b. To put these differences in an application perspective, it is only necessary to appreciate that the ionospheric conductivities are dependent upon the *E* region densities. Hence, the magnitude of the Figure 4 *E* region difference map into differences in Hall and Pedersen conductivities. From Figure 4, noon at BLO case Hall conductivities are 8.5, 10.4, and 9.1 mho, respectively, for EUVAC, EVE-1 nm, and EVE-5 nm cases. The Pedersen conductivities are 8.7, 8.4, and 8.3 mho, respectively, for EUVAC, EVE-1 nm, and EVE-5 nm cases. The conductivity ratio, Hall/Pedersen are 0.98, 1.24, and 1.10 for the EUVAC, EVE-1 nm, and EVE-5 nm cases.

4.2. *E* and *F1* Region Sensitivity Study

[25] Today, our empirical knowledge of the solar irradiance spectrum that is relevant to the ionosphere is progressing toward a level of 24/7 observations and wide

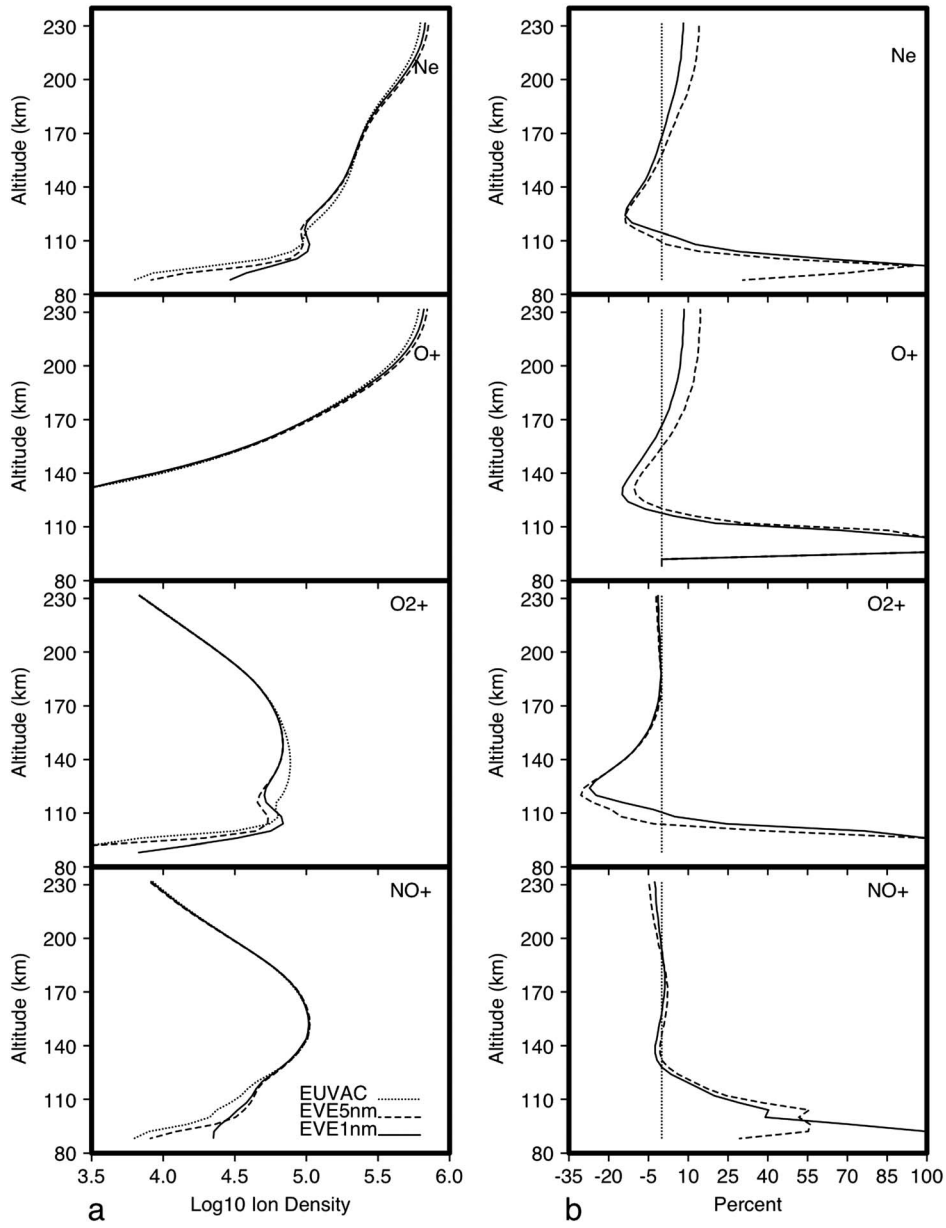

Figure 4. Expands the *E* and *F1* region for the TDIM simulations shown in Figure 3 with the lower altitude of the simulations being 88 km. Both the left panels' logarithmic density scale and the right panels' percentage difference scales have been adjusted to the *E* layer ranges.

spectral coverage at a very high time resolution. This opens the possibility of detailed ionospheric modeling in which the *E*, *F1*, and *F2* regions have each their own characteristic responses to specific portions of the spectrum. The solar irradiance modeling work of *Chamberlin et al*. [2008] points out the need for this high-resolution database, especially during solar flare conditions, when the shortest XUV wavelengths readily vary by more than two orders of magnitude, while the longest ionizing wavelengths reach a factor of 2 in their variability. Since the cross sections are smallest at both the short and long wavelengths, these two ends of the XUV-EUV spectrum penetrate to the lower altitudes and, in fact, are the dayside source of the *E* and *F1* regions.

[26] Observations made by the Student Nitric Oxide Explorer (SNOE) provided evidence that the XUV irradiance had been very much underestimated [*Bailey et al*., 2000]. The SNOE Solar X-ray Photometer (SXP) had three primary spectral ranges: 2–7, 6–19, and 17–20 nm. *Solomon et al*. [2001] showed that the irradiances in these ranges, as measured by SNOE, were 2 to 10 times larger than the estimates that had previously been used in ionospheric modeling. Their model of the *E* and *F1* regions, using the SNOE irradiances, provided agreement with ionospheric measurements of the ISR at Millstone Hill, Massachusetts. Thus, the SNOE mission provided strong evidence pointing to the need for 24/7 observation of the XUV spectrum. In the following subsections, we use the TDIM model to see how sensitive the *E* and *F1* regions are to the XUV irradiance. We adopt as our standard EUV model the EVE 1 nm resolution presentation.

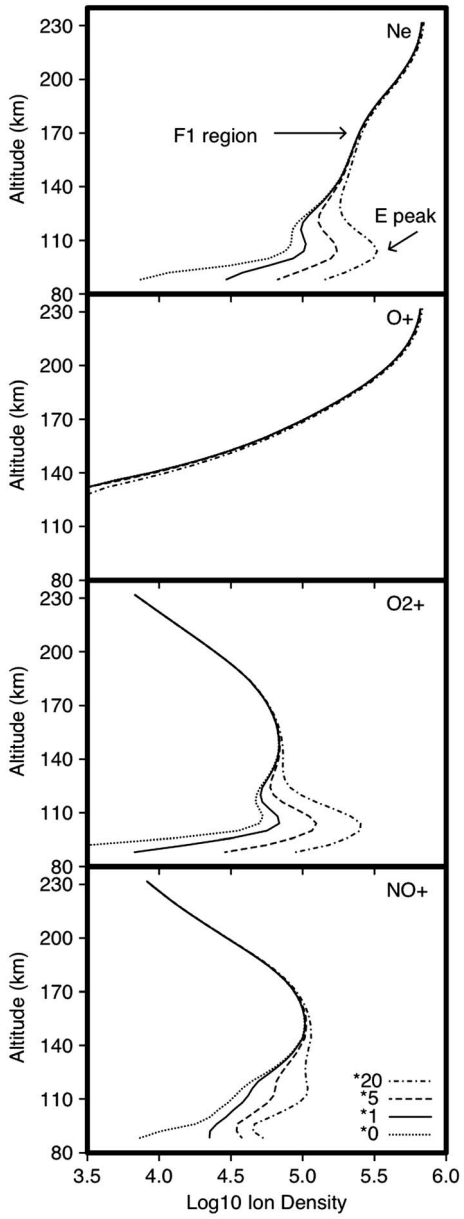

Figure 5. TDIM *E* and *F1* region simulations for the standard EVE spectrum (solid lines) with three additional sensitivity simulations in which the 0.1 to 5 nm irradiance is scaled by 0, 5, and 20. The lower three panels represent the ion densities as a function of altitude at noon on 8 February 2012 at BLO location. A key in the lower panel identifies the sensitivity scaling factors, and the ions are NO^+, O_2^+, and O^+ starting from the bottom panel. The corresponding electron density profile is shown in the upper panel (Ne).

4.2.1. *E* and *F1* Sensitivity at 2 to 5 nm

[27] The XUV irradiance in the range 2–5 nm is the most challenging to specify because at this time, no observations are available that have anywhere near the high resolution offered by MEGS-A and MEGS-B. It is this very wavelength range, according to *Chamberlin et al*. [2007, 2008], which exhibits more than an order of magnitude change in irradiance as well as a marked change in spectral shape during solar flare conditions and also over the 11 year solar cycle.

[28] For the TDIM simulations in this sensitivity study, a standard EVE spectrum is taken on 8 February 2012, representing quiet solar conditions during a campaign when the full MEGS-A and MEGS-B were operating for 12 h. As indicated earlier, the ESP-QD integrated irradiance from 0.1 to 7 nm needs to be distributed over the 2–5 and 5–10 nm bins. To do this accurately, the spectral shape in the 0.1 to 7 nm region would have to be known, and of course, this is precisely the information that is lacking. The simplest method is to assume a flat spectral shape; to estimate the amount of error that might result from such an assumption, we carried out a large number of TDIM simulations with a wide variety of artificially produced spectral shapes. We found

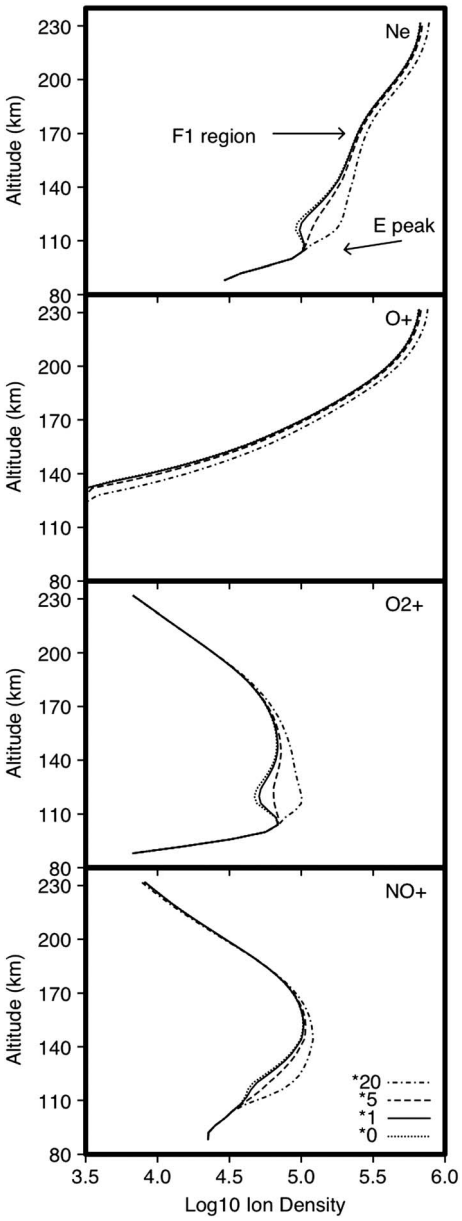

Figure 6. TDIM *E* and *F1* region simulations for the standard EVE spectrum (solid lines) with three additional sensitivity simulations in which the 10 to 15 nm irradiance is scaled by 0, 5, and 20. Otherwise, the format is identical to that in Figure 5.

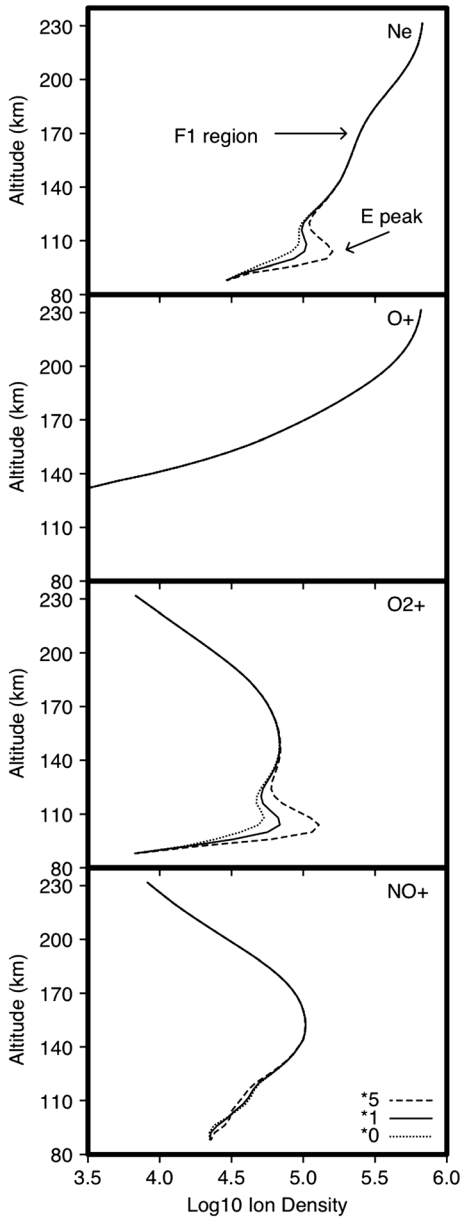

Figure 7. TDIM *E* and *F1* region simulations for the standard EVE spectrum (solid lines) with two additional sensitivity simulations in which the 100 to 105 nm irradiance is scaled by 0 and 5. Otherwise, the format is identical to that in Figure 5.

that the maximum variability in the *E* and *F1* regions resulting from this variation in spectral shape was no more than 20% and that this highest variability was found in the density within the valley region, that is, between the *E* and *F1* regions. Hence, for this study, we redistribute the ESP-QD irradiance according to a flat spectral shape, acknowledging a 10%–20% valley region error during solar flares.

[29] For this sensitivity study, the TDIM was run for the location of BLO, in Utah, at local noon. Solar and geomagnetic conditions were quiet (Kp = 1, F10.7 = 95, F10.7A = 119). In addition to the basic model run with the quiet time solar spectrum, the irradiance values input to the TDIM in the 2 to 5 nm range were multiplied by factors of 5, 20, and zero. The selection of the numbers 5 and 20 for the multiplying factors was based on the work of *Chamberlin et al*. [2008], specifically their Figure 2, as roughly corresponding to their X17 and X28 flares, respectively.

[30] Figure 5 shows the results of the four TDIM simulations, with the solid-line curves representing the basic case with the standard EVE spectrum. The graph in the upper panel shows the profiles of electron density (Ne) on a logarithmic scale; individual species O^+, O_2^+, and NO^+ are shown in the other three panels. We see a distinct *E* region peak around 108 km. An *F1* region exists between 125 and 180 km; a clear peak is seen only in the species NO^+, at an altitude of about 160 km.

[31] For the model run in which the solar irradiance spectrum from 2 to 5 nm has been set to zero, represented by the dotted line curves in Figure 5, the impact on O^+ is negligible, but for NO^+ and O_2^+ and in the *E* region and valley, a decrease of about 30% is present. It can also be noted that photons in this wavelength band have enough energy to generate multiple secondary ionizations; in some cases, in excess of 20 secondary ionizations can take place.

[32] The two model runs in which the irradiance spectrum from 2 to 5 nm has been multiplied by 5 and 20, are represented by the dashed and chain-dotted lines, respectively. The *E* region responds with an increase in density, in NO^+ and O_2^+; there is an increase of almost a factor of 4 in electron density in the case of scaling by 20 for O_2^+ and an increase in density for NO^+ by a factor of 2.5. Even when the 2 to 5 nm irradiance value is multiplied by 20, it has almost no effect in the *F1* region (and no effect whatsoever in the *F2* region, not shown in Figure 5). This wavelength range is a major *E* layer ionization source.

4.2.2. *E* and *F1* Sensitivity at 10 to 15 nm

[33] The sensitivity study just described was repeated, with the same set of multiplying factors, but this time with the solar irradiance spectrum in the range of 10 to 15 nm being scaled; the results are given in Figure 6. *Chamberlin et al.* [2008] reported that this wavelength band has a very high degree of variability during solar flares, similar to the 2 to 5 nm band, and this result has been confirmed with the MEGS-A spectral measurements. The solid line case, again the unscaled TDIM run, is of course identical with that shown in Figure 5. However, the results of the sensitivity study are very different. This wavelength band has little to no effect on the *E* region peak; rather, the contribution is to the valley and the *F1* region. The magnitude of the change effected by scaling this wavelength band is significantly less than it was in the 2 to 5 nm case; the largest effect is about a factor of 2.

[34] We have also studied the effect of scaling the irradiances in the wavelength range of 5–10 nm and 15–20 nm, but we do not show results in a figure. In the case of 5 to 10 nm, these wavelengths show rather little response to solar flare conditions [see *Chamberlin et al*., 2008, Figure 6]. In the case of 15 to 20 nm, these photons do not penetrate to the altitude range we are focusing upon, and the ionization occurs mostly within the *F2* layer.

4.2.3. *E* and *F1* Sensitivity at 100 to 105 nm

[35] Photoionization of N_2 and O does not occur for wavelengths above 80 and 91 nm, respectively. However, photoionization of O_2 does occur at wavelengths up to 103 nm. Above 90 nm, the O_2 ionization cross sections are

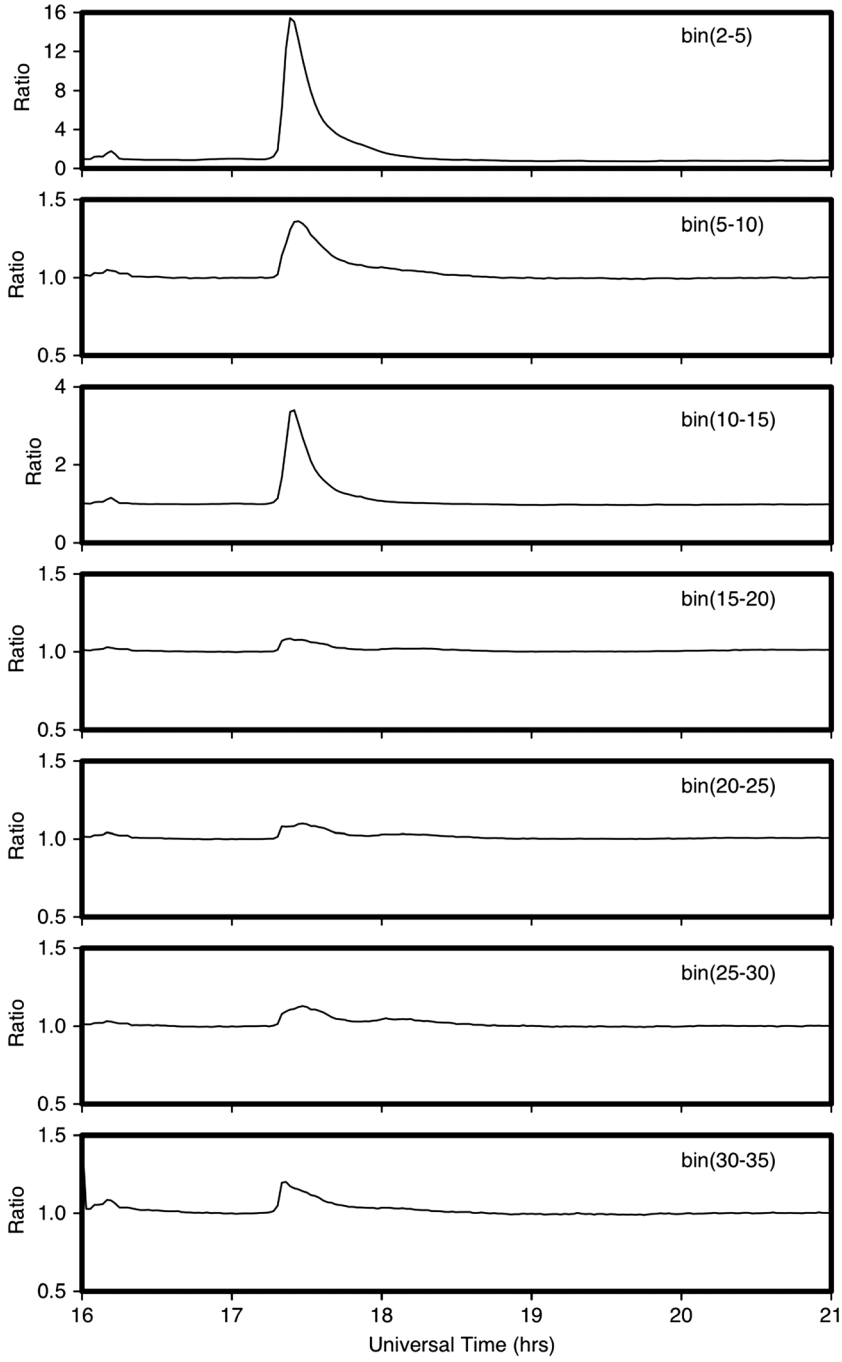

Figure 8. Time development of the X1.6 flare irradiances for seven 5 nm bins. The irradiance increase relative to the quiet solar irradiance for each bin is plotted as a ratio.

small, thus resulting in ionization within the *E* and *F1* regions. As before, TDIM simulations were done to find out how much ion densities are changed by scaling the irradiance values within this range. Note, however, that we use different scaling factors here, just 0 and 5 instead of 0, 5, and 20. Again, we cite the study by *Chamberlin et al*. [2008]; their Figure 2 shows that the irradiance in this longer wavelength range is not expected to vary by more than about a factor of 2. Figure 7 shows the results of the TDIM runs, as altitude profiles at local noon for the 100 to 105 nm sensitivity study. There is no effect whatsoever upon the density profile of O^+. There is a significant effect upon O_2^+ in the area of the *E* region peak and also the valley. The degree of variation near the peak approaches a factor of 2.5. It is interesting to note that these photons do not ionize N_2; there is nonetheless an inverse effect upon the NO^+ density profile in the valley region due to chemical reactions.

[36] The electron density plot in Figure 7 (top) shows that this band does provide significant ionization in the *E* region; however, the intensity in this band is increased only mildly during solar flare conditions. When modeling the complex process of ionization cascades, it is important to keep in mind

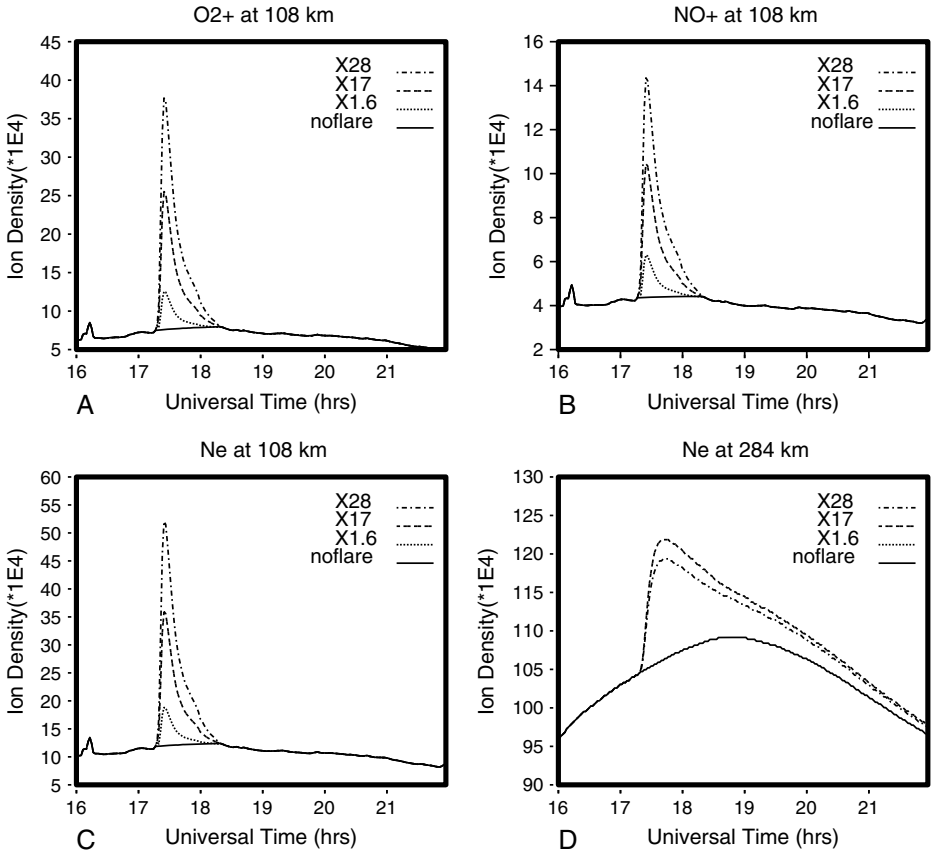

Figure 9. (a) Simulated ionospheric O_2^+ density at 108 km for the quiet Sun irradiance (solid line), X1.6 flare (dotted line), X17 flare (dashed line), and X28 flare (dashed dotted line). The temporal evolution of the flare simulations follows that of the flare time axes shown in Figure 8. 19:00 UT corresponds to local noon at the BLO location. (b) Simulated ionospheric NO^+ densities at 108 km. (c) Electron densities at 108 km. (d) *F2* electron density with its contrasting time evolutions.

that the photoelectrons released by ionizations in this wavelength band do not have enough energy to produce any secondary ionization.

4.3. May 2011 Flare and Flare Sensitivity

[37] Since the launch of the SDO, a number of lesser X-class flares have been observed. To study the sensitivity of the *E* and *F1* regions to solar flares, we use the flare that was observed on 9 March 2011 as our EVE flare example but with the caveat that we have changed the onset time of the flare so that it occurs when the BLO location is near local noon. This was an X1.6 level flare; there was a well-defined quiet solar irradiance spectrum both before and after the event. In Figure 8, we show the evolution of this flare in the first seven wavelength bins of our 22-bin scheme; we plot the ratio of the irradiance for the flare condition to the irradiance for the quiet condition. The flare is initiated at the shifted BLO time, 17:20 UT, and reaches a peak between 5 and 10 min later.

[38] Even at the broad resolution of the 5 nm bins, it is easily seen that the flare has a very different effect upon different parts of the spectrum. The largest effect is in the first bin, 2 to 5 nm, in which the irradiance is increased by about a factor of 15. Consistent with the earlier discussion (in section 4.2.1), there is little effect in the next bin of 5 to 10 nm and then again a significant effect at 10 to 15 nm. Beyond this bin, the effect ranges between 10% and 20%.

[39] Before the EVE operational period, the TIMED SEE instrument did capture some X-class flares that were considerably larger than any that have yet been seen by EVE. Two in particular, an X17 and an X28, have been studied in detail and form the basis of the Flare Irradiance Solar Model (FISM) [*Chamberlin et al*., 2008]. It is interesting that at wavelengths above 30 nm, the irradiance increase during the X17 flare is quite a bit larger than the increase that was seen during the X28 flare. This inverted relationship, in which the weaker flare may have the greater irradiance in the long wavelength band, is a further complication in the modeling of the solar spectrum. In this case, *Chamberlin et al*. [2008] attribute this inverted relationship to the relative location of these two flares on the solar disk, with the X28 flare being on the limb, and hence the different degrees of absorption to which these wavelengths are subjected in the solar atmosphere.

[40] With the TDIM model, again for the BLO location at local noon, we carried out a sensitivity study to assess the effect of the three flares, the X1.6, X17, and X28, relative to quiet solar conditions. To do this, we scaled in each case every bin of the solar spectrum by the appropriate factor as determined by the flare observations. For the two large flares,

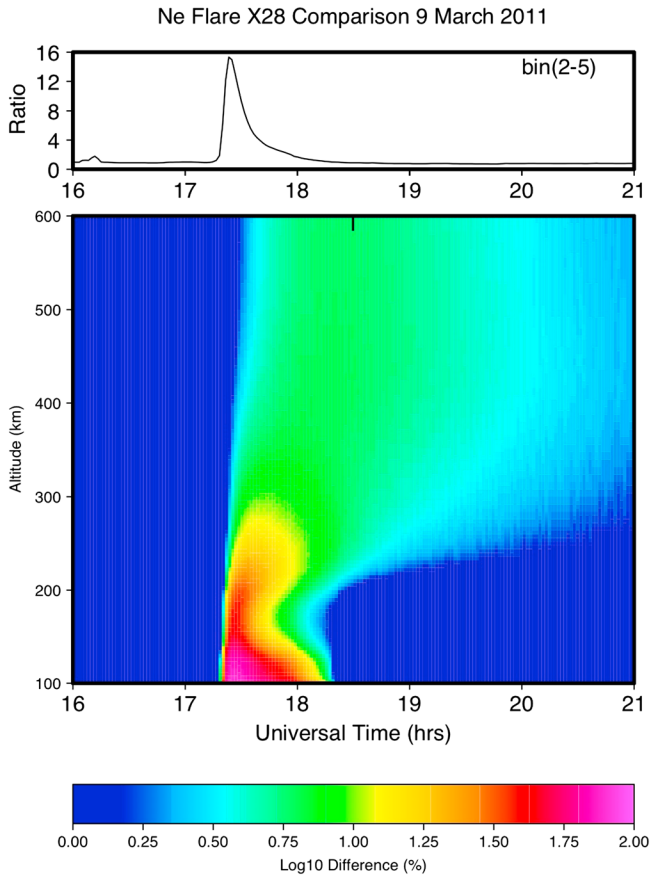

Figure 10. Simulated response of the ionospheric electron density to the X28 flare. The electron density response is shown as the logarithm of the percentage difference between the flare and the quiet Sun electron densities. Red is the highest percentage, where 1.75 corresponds to a 56% increase. The top panel shows the time evolution of the 2 to 5 nm irradiance bin.

the scaling factors were read from Figure 2 of the study by *Chamberlin et al*. [2008]. We give results in Figure 9a-d, in which we plot, this time on a linear scale, the ion or electron densities as a function of time. In each case, the solid curve represents the quiet Sun case. This curve for the no-flare case shows only the diurnal variation in density that results from the changing solar zenith angle as the ionospheric location being modeled corotates through the dayside region. Figure 9a shows the modeled O_2^+ densities at an altitude of 108 km; this altitude was chosen as being representative of the *E* region peak. On the dayside at this altitude, the time constant for ionospheric change is less than 1 min; hence, the *E* region is responding directly to changes in irradiance. The three cases of X-class flares all provide a time evolution like that of the flare shown in Figure 8. The increases in the O_2^+ peak for the X1.6, X17, and X28 flares, respectively, are factors of 1.8, 3.6, and 5.3.

[41] Figure 9b shows the NO^+ densities at 108 km, for the same model runs as Figure 9a. The NO^+ densities also respond directly to the flare risetime, and the factors of increase over no flare conditions are 1.4, 2.3, and 3.2, respectively, for the X1.6, X17, and X28 flares. Figure 9c shows the modeled electron density (Ne) response to these flares. All three of these panels, 9a, 9b, and 9c, show the *E* region responding directly to the solar flare dynamics.

[42] Although in this paper, we focus on the *E* and *F1* regions, we will present some results of this sensitivity study within the *F2* region, where, because of the much longer time constants, the response to a flare is dramatically different [see, eg., *Smithtro et al*., 2006]. In Figure 9d, we show the electron density Ne at the *F2* region altitude of 284 km for the same four flare scenarios as in the preceding figures. This altitude is close to the typical *F* region peak and is in an altitude range where O^+ is the dominant ion. It takes somewhat longer for the peak response to occur, about 15 min; this is longer than either the flare risetime or the *E* region response time. This difference can be seen by comparing the electron density shown in Figure 9c with that in Figure 9d. Much more significant than this increase in the time taken to reach the peak effect is that the decay time thereafter is much longer; in the *E* region, the effect of the flare was sudden and short-lived, but in the *F* region, it lasts for hours.

[43] The four scenarios point out the fact that there is a strong difference in the way that the various altitude regions of the ionosphere respond to a solar flare. This is a level of complexity that exists in addition to the already known fact that different wavelength bands have different responses to a flare. In Figure 10, we show the time evolution of the altitude profile of electron density in the case of the X28 flare; color is used to show the logarithm base 10 of the percentage

increase relative to the TDIM simulation for quiet conditions. The dynamic range of the color key ranges from 1% to 100%. The *E* region has differences that for the peak Ne, reached a factor of 4.5, see Figure 9c. this would correspond to a 350% difference and a $\log_{10}$ difference of 2.54. Between 100 and 108 km, the ionosphere is responding directly to the flare, while at higher altitudes, a delay in ionization buildup is seen, the delay becoming longer as altitude is increased.

[44] The *F2* layer electron density temporal evolution is significantly different from that of the lower *E* and *F1* region. Above 200 km, the *F2* flare response is no longer in step with the XUV irradiance but is delayed. The amount of delay increases with altitude, see Figure 10 above 200 km. As the flare irradiance reaches its peak, the *F2* layer electron density is still increasing. In the *F2* region, the chemistry (production-loss) balance is augmented by diffusion. This in turn modifies the dynamics of the plasma leading to time constants reaching 1 h above the *F2* peak. Figure 10 shows the electron density increase being still significant at altitudes above 300 km 1 h after the flare irradiance (top panel, Figure 10) has returned to preflare levels. At 450 km, Figure 10, the maximum percentage increase in the electron density occurs at about 18:30 UT, which is >1 h after the flare irradiance has peaked. This particular delay between ionospheric response and the flare irradiance introduces a significant challenge in how best to introduce flare dynamics into ionospheric modeling, specification, and forecasting. The specific time evolution does not only depend on the ionosphere but also the specific wavelength dependence of the irradiance. This latter requirement is the major space weather contribution of the SDO-EVE instrument.

5. Discussion

[45] The TDIM simulations that compared the noon BLO ionospheric profiles for three solar irradiance representations provide a realistic state of dayside-midlatitude ionospheric modeling. In the *F* region, 200–500 km, these simulations are within 15% of each other or on this day have a TEC spread 1.3 tecu. This might not seem important except that accurate knowledge of the TEC to better than a tecu is being strived for as GPS applications become more demanding of better ionospheric corrections. A very obvious case is airline travel, most of which is during daylight hours. Present day methods to provide ionospheric TEC knowledge include assimilation models that combine ionospheric first principle models and ionospheric measurements. The final assimilation product depends on uncertainties in both the model and observations. Typically, the assimilated TEC will have 1 to 2 tecu uncertainty and other observations at least 10%. Section 4.1 results indicate that at least a similar uncertainty is introduced into the ionospheric models by virtue of having to use a solar irradiance. The challenge is ongoing; assimilation of model research is to minimize these uncertainties. Hence, using the EVE irradiance measurements, their calibration and subsequent TDIM, or other ionospheric models, electron density profile validation will provide accurate knowledge of the solar X-EUV driver ionospheric impact.

[46] The SDO-EVE solar irradiance database, due to it high spectral resolution and continuous solar observation, provides an unprecedented specification of the ionizing photon flux for the *E* and *F1* layers. Previous authors, in works cited in this paper, have demonstrated the importance of the XUV irradiance in generating the *E* and *F1* regions. These studies, as well as the present, indicate clearly that the irradiance spectrum from 2 to 15 nm controls the relative magnitudes of the *E*, *F1*, and valley regions both in absolute density and in ion composition. Here we have additionally emphasized the relevance of the 90 to 103 nm photons since they produce O_2 ionization; unlike the shorter wavelength bands, the resulting photoelectrons are incapable of causing secondary ionizations. This longer wavelength produces O_2^+ and through chemistry this leads to a decrease in the other major molecular ion NO^+.

[47] When specifying the cascade of secondary ionization in the ionospheric model used in this study, we use the generally agreed upon "35 eV" scheme of *Rasmussen et al.* [1988] in which secondary ionization is found by calculating the "extra" energy given to these photoelectrons to produce more ionizations requiring them to have at least 35 eV. Other researchers have used different approaches. *Lilensten et al.* [1989] employed a first principles photoelectron degradation code to generate scaling factor profiles; *Anderson et al.* [1998] used the generally agreed upon "PRIMO" formulations, in which photoionization is multiplied by a factor of 2 at all altitudes within the *E* region; *Solomon et al.* [2001] made use of SNOE data to rescale the standard XUV irradiance by a factor of 4 in addition to a factor for scaling due to energetic photoelectrons. In all of these studies, including our own, important missing elements are associated with the handling of ionization by the energetic photoelectrons, most notably a model of secondary electron transport.

6. Summary

[48] In this study, we have taken a step toward determining how much information about the XUV-EUV irradiance spectrum is necessary for ionospheric modeling to adequately describe the daytime *E* and *F1* regions. We see that today's knowledge of the XUV spectrum, which has been so much improved by the SDO-EVE data in both time cadence and spectral resolution, still leaves a need for better XUV coverage. In particular, spectral resolution of the band from 0.1 to 6 nm is required.

[49] By comparing the widely used semi-empirical EUVAC solar irradiance with two representations of the EVE irradiances, an ionospheric sensitivity to these three inputs was obtained. Over the whole *F2* region, the simulations differed by over a range of 5%–15%. In the lower *E* and *F1* region, the differences were significantly more altitude dependent and had larger magnitudes.

[50] The continuous observation at a 10 s cadence from the EVE instrument makes available a new input for ionospheric weather modeling, specifically solar flare events. In the *E* and *F1* regions, the time constants are on the order of a minute or longer; hence the EVE observations provide, for the first time, the temporal dynamics of the irradiance spectrum at a level which is suitable for driving the *E* and *F1* regions. To make best use of this input, ionospheric models will need to incorporate photoelectron transport codes; this is a future major development for space weather *E* and *F1* region models. Future research will also include obtaining observations of the *E* and *F* region with sufficient height resolution and

density accuracy to validate the progress being made using EVE irradiances and physical models of the ionosphere. These ionospheric measurements can best be made using incoherent scatter radars (ISR) operating in very specialized *E* region modes. This necessitates the synchronization of ISR measurements with SDO-EVE full spectral range observations. A first such joint campaign was held on 8/9 February 2012, and subsequent campaigns are being planned. The analysis of this first campaign is under way.

[51] **Acknowledgments.** This research was supported by NSF grant ATM-0408592 and NASA grant NNG04GNG3G to Utah State University and by NASA contract NAS5-02140 to University of Colorado.

[52] Robert Lysak thanks the reviewers for their assistance in evaluating this paper.

References

Anderson, D. N., et al. (1998), Intercomparison of physical models and observations of the ionosphere, *J. Geophys. Res.*, *103*, 2179–2192.

Bailey, S. M., T. N. Woods, C. A. Barth, S. C. Solomon, L. R. Canfield, and R. Korde (2000), Measurements of the solar soft x-ray irradiance from the Student Nitric Oxide Explorer: First analysis and under flight calibrations, *J. Geophys. Res.*, *105*, 27,179–27,193.

Banks, P. M., and G. Kockarts (1973), *Aeronomy*, Academic, New York.

Buonsanto, M. J., S. C. Solomon, and W. K. Tobiska (1992), Comparison of measured and modeled solar EUV flux and its effect on the E-F1 region ionosphere, *J. Geophys. Res.*, *97*, 10,513–10,524.

Chamberlin, P. C., T. N. Woods, and F. G. Eparvier (2007), Flare irradiance spectral model (FISM): Daily component algorithms and results, *Space Weather*, *5*, S07005, doi:10.1029/2007SW000316.

Chamberlin, P. C., T. N. Woods, and F. G. Eparvier (2008), Flare irradiance spectral model (FISM): Flare component algorithms and results, *Space Weather*, *6*, S05001, doi:10.1029/2007SW000372.

Fennelly, J. A., and D. G. Torr (1992), Photoionization and photo-absorption cross sections of O, N_2, O_2 and N for aeronomic calculations, *At. Data Nucl. Data Tables*, *51*, 321–363.

Hedin, A. E., et al. (1991), Revised global model of thermosphere winds using satellite and ground-based observations, *J. Geophys. Res.*, *96*, 7657–7688.

Hedin, A. E., M. J. Buonsanto, M. Codrescu, M.-L. Duboin, C. G. Fesen, M. E. Hagan, K. L. Miller, and D. P. Sipler (1994), Solar activity variations in the midlatitude thermospheric meridional winds, *J. Geophys. Res.*, *99*, 17,601–17,608.

Hedin, A. E., et al. (1996), Empirical wind model for the upper, middle and lower atmosphere, *J. Atmos. Terr. Phys.*, *58*, 1421–1447.

Hinteregger, H. E., K. Fukui, and B. R. Gilson (1981), Observational, reference and model data on solar EUV, from measurements on AE-E, *Geophys. Res. Lett.*, *8*, 1147–1150.

Hock, R. A., P. C. Chamberlin, T. N. Woods, D. Crotser, F. G. Eparvier, M. Furst, D. L. Woodraska, and E. C. Woods (2012), EUV Variability Experiment (EVE) Multiple EUV Grating Spectrographs (MEGS) Radiometric Calibrations and Results, *Sol. Phys.*, *275*, 145–178, doi:10.1007/s11207-010-9520-9.

Lilensten, J., W. Kofman, J. Wisemberg, E. S. Oran, and C. R. Devore (1989), Ionization efficiency due to primary and secondary photoelectrons: A numerical model, *Ann. Geophys.*, *7*, 83–90.

Picone, J. M., A. E. Hedin, D. P. Drob, and A. C. Aikin (2002), NRLMSISE-00 empirical model of the atmosphere: Statistical comparisons and scientific issues, *J. Geophys. Res.*, *107*(A12), 1468, doi:10.1029/2002JA009430.

Rasmussen, C. E., R. W. Schunk, and V. B. Wickwar (1988), A photochemical equilibrium model for ionospheric conductivity, *J. Geophys. Res.*, *93*, 9831–9840.

Richards, P. G., J. A. Fennelly, and D. G. Torr (1994), EUVAC: A solar EUV flux model for aeronomic calculations, *J. Geophys. Res.*, *99*, 8981–8992, doi:10.1029/94JA00518.

Schunk, R. W. (1988), A mathematical model of the middle and high-latitude ionosphere, *Pure Appl. Geophys.*, *127*, 255–303.

Schunk, R. W., and J. J. Sojka (1982), Ion temperature variations in the daytime high-latitude F region, *J. Geophys. Res.*, *87*, 5169–5183.

Schunk, R. W., and J. C. G. Walker (1973), Theoretical ion densities in the lower ionosphere, *Planet. Space Sci.*, *21*, 1875–1896.

Schunk, R. W., P. M. Banks, and W. J. Raitt (1976), Effects of electric fields and other processes upon the nighttime high-latitude F layer, *J. Geophys. Res.*, *81*, 3271–3282.

Schunk, R. W., W. J. Raitt, and P. M. Banks (1975), Effect of electric fields on the daytime high-latitude E and F regions, *J. Geophys. Res.*, *80*, 3121–3130.

Schunk, R. W., J. J. Sojka, and M. D. Bowline (1986), Theoretical study of the electron temperature in the high-latitude ionosphere for solar maximum and winter conditions, *J. Geophys. Res.*, *91*, 12,041–12,054.

Smithtro, C. G., J. J. Sojka, T. Berkey, D. Thompson, and R. W. Schunk (2006), Anomalous F region response to moderate solar flares, *Radio Sci.*, *41*, RS5S03, doi:10.1029/2005RS003350.

Sojka, J. J. (1989), Global scale, physical models of the F region ionosphere, *Rev. Geophys.*, *27*, 371–403.

Sojka, J. J., W. J. Raitt, and R. W. Schunk (1981a), Theoretical predictions for ion composition in the high-latitude winter F region for solar minimum and low magnetic activity, *J. Geophys. Res.*, *86*, 2206–2216.

Sojka, J. J., W. J. Raitt, and R. W. Schunk (1981b), A theoretical study of the high-latitude winter F region at solar minimum for low magnetic activity, *J. Geophys. Res.*, *86*, 609–621.

Solomon, S. C., S. M. Bailey, and T. N. Woods (2001), Effect of solar soft X-rays on the lower ionosphere, *Geophys. Res. Lett.*, *28*, 2149–2152.

Titheridge, J. E. (1996), Direct allowance for the effect of photoelectrons in ionospheric modeling, *J. Geophys. Res.*, *101*, 357–369.

Torr, M. R., D. G. Torr, R. A. Ong, and H. E. Hinteregger (1979), Ionization frequencies for major thermospheric constituents as a function of solar cycle 21, *Geophys. Res. Lett.*, *6*, 771–774.

Woods, T. N., et al. (2012), Extreme Ultraviolet Variability Experiment (EVE) on the Solar Dynamics Observatory (SDO): Overview of science objectives, instrument design, data products, and model developments, *Sol. Phys.*, *275*, 115–143, doi:10.1007/s11207-009-9487-6.